

Synchrotron emission from nanowire-array targets irradiated by ultraintense laser pulses

B Martinez^{1,2}, E. d’Humières² and L. Gremillet¹

¹ CEA, DAM, DIF, F-91297 Arpajon, France

² CELIA, UMR 5107, Université de Bordeaux-CNRS-CEA, 33405 Talence, France

E-mail: bertrand.martinez@cea.fr, laurent.gremillet@cea.fr

Abstract. We present a numerical study, based on two-dimensional particle-in-cell simulations, of the synchrotron emission induced during the interaction of femtosecond laser pulses of intensities $I = 10^{21} - 10^{23} \text{ Wcm}^{-2}$ with nanowire arrays. Through an extensive parametric scan on the target parameters, we identify and characterize several dominant radiation mechanisms, mainly depending on the transparency or opacity of the plasma produced by the wire expansion. At $I = 10^{22} \text{ Wcm}^{-2}$, the emission of high-energy ($> 10 \text{ keV}$) photons attains a maximum conversion efficiency of $\sim 10\%$ for $36 - 50 \text{ nm}$ wire widths and $1 \mu\text{m}$ interspacing. This maximum radiation yield is found to be similar to that achieved in uniform plasma of same average (sub-solid) density, but nanowire arrays provide efficient radiation sources over a broader parameter range. Moreover, we examine the variations of the photon spectra with the laser intensity and the wire material, and we demonstrate that the radiation efficiency can be further enhanced by adding a plasma mirror at the backside of the nanowire array. Finally, we briefly consider the influence of a finite laser local spot and oblique incidence angle.

PACS numbers: 52.38.-r;52.65.Rr,81.07.Gf

keywords: relativistic laser-plasma interactions, particle-in-cell method, synchrotron radiation, nanowires

Submitted to: *Plasma Phys. Control. Fusion*

Introduction

Forthcoming multi-petawatt (PW) laser systems will enable scientists to access a new regime of laser-plasma interactions where radiative and quantum electrodynamics (QED) effects are strongly coupled with collective plasma processes [1]. On-target laser intensities in the $10^{22} - 10^{24} \text{ Wcm}^{-2}$ range are expected to be reached at several facilities—CILEX-Apollon [2], PULSER [3], ELI [4], Vulcan-10 PW [5] and XCELS [6], to name a few—, opening up exciting applications in fundamental and applied research, such as radiation pressure ion acceleration [7, 8, 9], the study of quantum radiation reaction on laser-driven electrons [10, 11, 12, 13, 14], the massive production of electron-positron pairs through the Breit-Wheeler process [15, 16, 17, 18, 19, 20, 21], or

relativistic laboratory astrophysics [22, 23, 24]. One fundamental mechanism common to all these applications is the copious generation of hard x-ray or γ -ray photons through synchrotron emission—equivalent to nonlinear inverse Compton scattering in the strong-field regime [25]. In recent years, experimental progress in this direction has been achieved by making ultrarelativistic electrons issued from a laser wakefield accelerator collide with an intense laser pulse [26, 27, 28, 29, 30, 31]. Furthermore, the capability of this configuration in yielding efficient pair creation at laser intensities $\gtrsim 10^{23} \text{ Wcm}^{-2}$ has been numerically [32] and theoretically [33] examined.

The particle-in-cell (PIC) simulation technique [34] is the most widely used tool for modeling the kinetic and collective phenomena at play in intense laser-plasma interaction. Recently, in order to prepare for multi-PW laser experiments, much effort has been expended in enriching PIC codes with numerical models describing synchrotron emission and multiphoton Breit-Wheeler pair production [35, 36, 37, 38, 39, 40, 41, 42, 43, 44]. Such upgraded codes are being extensively exploited to gain understanding of the radiation-modified laser-plasma interaction in various parameter ranges. In uniform plasmas, several radiation regimes have been identified depending on the laser intensity and plasma density. Above the relativistic critical density, an electromagnetic standing wave is formed at the laser-irradiated target front; the resulting synchrotron radiation (referred to as skin depth emission, SDE [17]) is mainly emitted in a forward-directed cone, yet remains relatively weak (with a $\lesssim 1\%$ conversion efficiency at laser intensities $I \sim 10^{22} \text{ Wcm}^{-2}$). In relativistically near-critical or undercritical plasmas, the radiation is predominantly emitted in the transverse (transversally oscillating electron emission, TOEE [45]) or in the backward direction (reinjecting electron synchrotron emission, RESE [46]). The radiation yield has been found to be maximized in the RESE regime, with a $\sim 1\%$ conversion efficiency predicted at $I \sim 10^{22} \text{ Wcm}^{-2}$ [47]. Strategies to enhance the synchrotron emission or improve its properties have been proposed, taking advantage of preplasmas [47], plasma channels [48, 49], or structured targets such as gratings [50], cone targets [19, 51, 52], clusters [53], micro-plasma waveguides [54], or nanowire arrays [55, 56, 57]. The purpose of the present paper is to further explore the potential of the latter target type for high-energy synchrotron radiation.

The realization of intense laser-driven synchrotron sources is but the latest application of nanowire (or nanotube) arrays. Originally, their use was aimed at strongly increasing the absorption of moderately relativistic ($I \sim 10^{17} - 10^{19} \text{ Wcm}^{-2}$) short-pulse lasers into fast electrons, which can then drive bright Bremsstrahlung or x-ray line emission [58, 59, 60, 61, 62]. Such targets also allow for long-distance collimated transport of the fast electrons as a result of self-induced electromagnetic fields [63, 64, 65]. Moreover, fast-electron relaxation causes rapid volumetric heating and homogenization of the nanowires, thus creating extremely hot dense matter samples. Formation of plasmas of $\sim 10^{23} \text{ cm}^{-3}$ densities and $\sim 1 - 10 \text{ keV}$ temperatures, associated with pressures of a few Gbar, has thus been inferred by x-ray emission at $\sim 10^{19} \text{ Wcm}^{-2}$ laser intensities [66, 67]. The increased number and mean energy of the fast electrons enabled by nanowire arrays coated on thin solid foils have also proven beneficial for accelerating ions in the target normal sheath acceleration regime [68, 69]. One should stress, however, that these experiments raise the key issue of the laser contrast, which, if too low, may prevent the laser light from penetrating the interwire gaps [70].

Along with the aforementioned experimental works, a number of PIC simulation studies have examined the dependencies of the laser absorption and fast-electron

generation on the nanowire-array parameters [71, 72, 55, 56, 70]. These works suggest that the laser absorption can reach values as high as 90% at $I \sim 10^{19} - 10^{20} \text{ Wcm}^{-2}$ and interwire spacings in the $\sim 0.1 - 1 \mu\text{m}$ range. The possibility of triggering betatron electron acceleration in the superimposed laser and quasistatic fields around the wires has also been demonstrated under specific conditions (*e.g.*, a 10^{19} Wcm^{-2} laser pulse irradiating 60-nm-diameter wires) [55, 56]. These trends, revealed at relatively moderate laser intensities, make nanowire arrays promising setups for developing ultraintense synchrotron sources at extreme laser intensities, $I > 10^{22} \text{ Wcm}^{-2}$. Another argument in their favor is that the strong magnetostatic fields they give rise to (through the interplay of the fast electrons and the return current flowing inside the wires [73]) may, if sustained long enough, significantly enhance the synchrotron emission compared to that induced by the sole laser field. A similar scenario of synchrotron radiation boosted by quasistatic fields has been numerically evidenced in a plasma channel [48].

In the work reported here, based on 2D simulations performed with the PIC-QED code CALDER [42], we investigate the dominant processes of synchrotron emission and their properties as a result of the interaction of an ultraintense ($10^{21} \leq I \leq 10^{23} \text{ Wcm}^{-2}$), ultrashort (30 fs) laser pulse with a nanowire array of varying geometry. Our paper is organized as follows. In Sect. 1, a reference scenario is presented, which considers a stand-alone nanowire array and serves to illustrate the main stages of photon emission. In Sect. 2, we perform a parametric scan where we vary the wire interspacing, width and atomic composition as well as the laser intensity. Our broad parameter range covers the transition from a regime where the structure of the nanowire array is maintained during the laser irradiation to a regime where it is destroyed early in the laser pulse, hence forming an essentially uniformized plasma. In addition, we compare the performance of nanowire arrays with that of uniform plasmas with varying density. In Sect. 3, we show that placing a solid foil at the backside of the nanowire array can notably increase the photon source efficiency (in case of significant laser transmission through the nanowires). Section 4 addresses the changes brought by a finite laser spot size and an oblique incidence angle. Finally, we summarize our results and suggest possible follow-up studies.

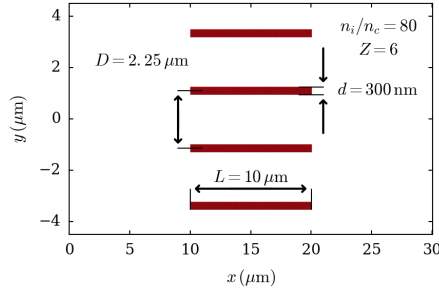


Figure 1. Schematic of the reference simulation setup.

1. Main synchrotron emission processes in laser-nanowire-array interactions

1.1. 2D PIC simulation setup

In this Section, we show that the synchrotron radiation proceeds through various stages during the interaction of an ultraintense laser pulse with a nanowire array. This is done in light of a reference 2D PIC simulation parameterized as follows. The laser pulse is modeled as a planar electromagnetic wave, propagating along the x axis, linearly polarized along the y direction and with a central wavelength $\lambda_0 = 1 \mu\text{m}$. It has a Gaussian temporal profile with a FWHM duration of 30 fs and a peak intensity $I = 10^{22} \text{Wcm}^{-2}$ (corresponding to a dimensionless field strength $a_0 = 85$). As depicted in Fig. 1, the target consists of a periodic array of solid-density carbon nanowires. The carbon atoms, of atomic number $Z = 6$, and mass number $A = 12$, are initially ionized with an atomic density $n_C = 80n_c$ ($n_c \simeq 1.1 \times 10^{21} \text{cm}^{-3}$ is the nonrelativistic critical density). The wires have a length $L = 10 \mu\text{m}$, a width (diameter in 3D) $d = 0.3 \mu\text{m}$ and the interwire spacing is $D = 2.25 \mu\text{m}$. The wire width is equal to that considered in Ref. [73], where it was shown to give rise to strong quasistatic fields at $I = 5 \times 10^{21} \text{Wcm}^{-2}$ (for circular polarization). The absence of a substrate at the backside of the wires, which could absorb and reflect the laser pulse, allows us to isolate the effects induced by the sole wires. The simulation domain has dimensions $L_x \times L_y = 30 \mu\text{m} \times 9 \mu\text{m}$, with a spatial resolution $\Delta x = \Delta y = \lambda_0/210$. The temporal resolution is $\Delta t = \tau_0/314$ (where $\tau_0 = \lambda_0/c = 3.3 \text{fs}$ is the optical cycle) and the simulation is run over $25000\Delta t$. The boundary conditions are taken to be absorbing along x and periodic along y for both fields and particles, and 50 macro-particles per cell and per species are used. The peak of the laser pulse hits the tips of the wires at time $t = 0$.

This illustrative simulation, as every other performed in this study, takes into account Coulomb binary collisions between charged particle species, field and impact ionization and synchrotron radiation. The synchrotron module implemented in CALDER [42] combines a continuous radiation reaction model [74] for electrons with a low quantum parameter ($\chi_e \leq 10^{-3}$) and a stochastic quantum description [37] for electrons with a higher quantum parameter ($\chi_e \geq 10^{-3}$). We recall that the electron quantum parameter, which determines the radiation characteristics, is defined as $\chi_e = \gamma[(\mathbf{E}_\perp + \mathbf{v} \times \mathbf{B})^2 + E_\parallel^2/\gamma^2]^{1/2}/E_S \simeq \gamma|\mathbf{E}_\perp + \mathbf{v} \times \mathbf{B}|/E_S$, where \mathbf{v} is the electron velocity, γ its relativistic factor, \mathbf{B} is the magnetic field, \mathbf{E}_\parallel is the electric

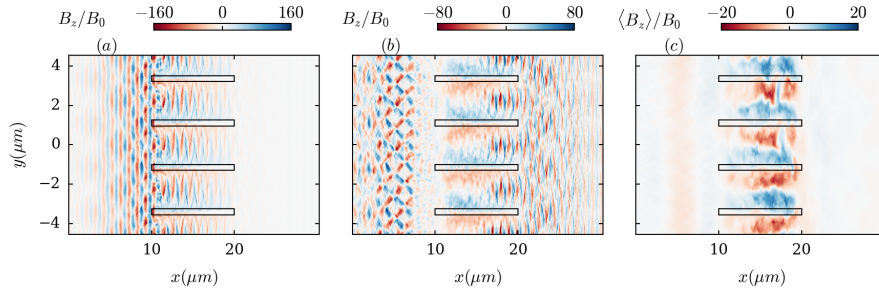


Figure 2. Maps of the magnetic field B_z (normalized to $B_0 = m_e \omega_0 / e \simeq 1.1 \times 10^4$ T) at three different times: (a) $t = 8$ fs (during plasma filling of the interstices), (b) $t = 40$ fs (after the left-hand side of the plasma-filled interstices have become opaque to the laser) and (c) $t = 167$ fs (final simulation time). The peak of the laser pulse hits the wire tips at $t = 0$. Panel (c) displays the magnetostatic field, $\langle B_z \rangle$, averaged over an optical cycle. The black rectangles plot the initial location of the wires.

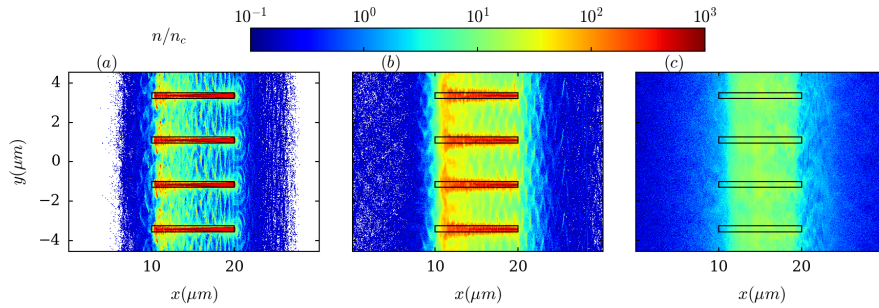


Figure 3. Maps of the electron density n_e (normalized to the nonrelativistic critical density $n_c \simeq 1.1 \times 10^{21}$ cm $^{-3}$) at (a) $t = 8$ fs and (b) $t = 40$ fs. Panel (c) displays the ion density n_i at $t = 167$ fs (final simulation time).

field component parallel to \mathbf{v} , \mathbf{E}_\perp the electric field component normal to \mathbf{v} , and $E_S = m_e^2 c^3 / \hbar e = 1.3 \times 10^{18}$ Vm $^{-1}$ is the Schwinger field [1]. The chosen threshold value between the two regimes is quite arbitrary, yet ensures that the quantum regime is accurately described. Pair production from Breit-Wheeler and Bethe-Heitler processes is neglected. For this reason, and in order to reduce the computational load, the radiated photons are not advanced on the simulation grid (but their energy and emission angle are recorded).

1.2. Typical dynamics of the laser-nanowire-array interaction and its associated synchrotron emission

Figures 2(a-c) display maps of the magnetic field (B_z) at three successive times, visualizing the penetration of the laser wave through the interwire gaps and the generation of quasistatic fields. The magnetic field is normalized to $B_0 = m_e \omega_0 / e = 1.1 \times 10^4$ T (where m_e is the electron mass, e is the elementary charge, and ω_0 is the laser angular frequency). The expansion dynamics of the wires is illustrated by the electron and ion density maps shown in Figs. 3(a-c). At the beginning of the

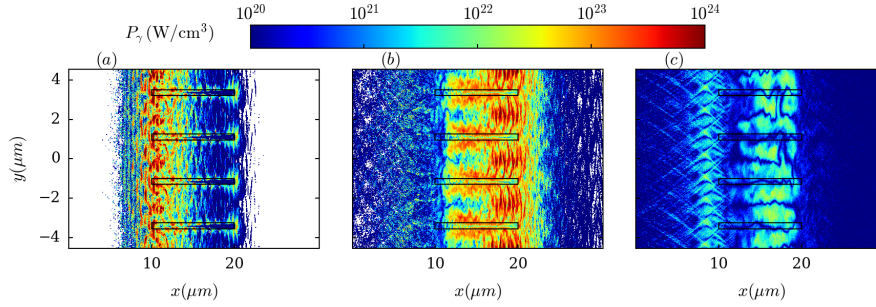


Figure 4. Maps of the radiated power density, P_γ , at three different times: (a) $t = 8$ fs (during plasma filling of the vacuum gaps), (b) $t = 40$ fs (after the left-hand side of the plasma-filled interstices have become opaque to the laser) and (c) $t = 167$ fs (final simulation time).

interaction, the electrons are pulled over a $\sim 1 \mu\text{m}$ distance from the wire surface by the E_y component of the laser field, and accelerated in the forward direction by its B_z component. As a result, the interwire gaps are filled with a population of energized electrons bunched at the laser wavelength λ_0 . Figure 3(a) is recorded shortly after the on-target laser peak ($t = +8$ fs), at which time the electron density in the interstices near the tips of the wires is of $\sim 50n_c$, *i.e.*, approaches the relativistic critical density $n_{cr} \simeq a_0 n_c$ (see also Sec. 2.4). Figure 2(a) shows that, up to this time, the interstices have remained (partially) transparent to the laser wave. The hot-electron current flowing in the interstices induces a magnetostatic field that is screened inside the wires by a return current carried by bulk electrons (of density $n_e \simeq Zn_C = 480n_c$). The amplitude of this field can be estimated by noting that the laser-accelerated electrons are initially extracted from a layer of thickness $\delta_{acc} \simeq a_0(n_c/n_e)c/\omega_0 \simeq 30$ nm (assuming immobile ions and a balance between the transverse laser and space-charge fields). These electrons generate a magnetostatic field of normalized strength $\langle B_z \rangle / B_0 \simeq \langle v_x / c \rangle (n_e / n_c) \delta_{acc} \omega_0 / c \simeq a_0 \langle v_x / c \rangle$, with $\langle v_x \rangle \simeq c$ the mean longitudinal fast-electron velocity. One therefore expects the strength of the self-induced magnetostatic field to be comparable with that of the laser field, in agreement with the maximum value $\langle B_z \rangle \simeq 0.7a_0$ measured at the laser peak. At laser intensities (resp. wire width) high (resp. small) enough that $\delta_{acc} \gtrsim d/4$, the number of electrons remaining inside the wires becomes lower than those expelled by the laser, so that current balance between the forward-moving hot electrons and the backward-moving core electrons [73] can no longer be maintained in the vicinity of a wire. In the planar-wave case under consideration, this leads to $\langle B_z \rangle$ dropping with decreasing $d \lesssim 4\delta_{acc}$, from $\langle B_z \rangle / B_0 \simeq (n_e / n_c) d \omega_0 / 4c$ down to zero in the fully depleted regime ($d \lesssim 2\delta_{acc}$).

The magnetostatic field tends to deflect inwards the bulk electrons, resulting in the pinching of the wire cores [73]. This transverse magnetic compression occurs early in time, as shown in Fig. 3(a) where one can note a contraction of the wires compared to their initial position (solid black lines). Simultaneously, the space-charge sheath field $\langle E_y \rangle / B_0 c \simeq (n_e / n_c) \delta_{acc} \omega_0 / c$ transversely accelerates the ions from the outer wire regions, and hence an increasingly dense plasma progressively fills up the interwire gaps. At $t = +40$ fs, the bulk electrons have expanded enough to form in the wire interstices a relativistically overcritical plasma ($n_e \geq n_{cr}$) opaque to the laser

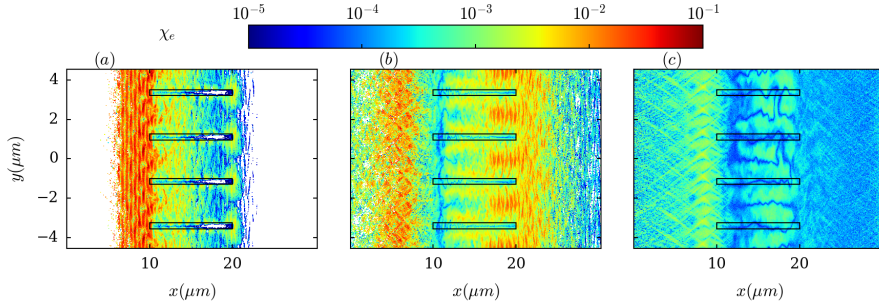


Figure 5. Maps of the electron quantum parameter, χ_e , at three different times: (a) $t = 8$ fs, (b) $t = 40$ fs and (c) $t = 167$ fs (final simulation time).

light [Fig. 3(b)]. This causes the splitting of the laser pulse into a transmitted part and a reflected one, as seen in Fig. 2(b). The density modulations at the plasma surface arising from the incomplete homogenization of the wires account for the reflection interference pattern seen in front of the target. Given the relatively large interwire spacing considered here, the laser transmission across the target is significant ($\simeq 13\%$). Figure 3 shows that, by $t = +167$ fs (about 85 fs after the laser pulse has exited the simulation domain), the nanostructure has been completely homogenized, the ion density then tending to the average density $n_i d/D = 11n_c$.

Figure 2(c) plots the quasistatic magnetic field $\langle B_z \rangle$, averaged over an optical cycle, at $t = 167$ fs. It demonstrates the relatively slow decay of the magnetostatic modulations sustained by the homogenized target electrons. At this instant, these modulations have a strength $\langle B_z \rangle \simeq 15B_0 \simeq 0.18a_0$, which remains an appreciable fraction of the laser field, and a typical variation length of $\sim 0.5 \mu\text{m}$, leading to magnetization of electrons with up to ~ 25 MeV energies, and therefore of the vast majority of the plasma electrons, of mean energy $\langle \gamma \rangle m_e c^2 \simeq 12$ MeV.

Let us now examine the synchrotron emission that takes place during and after the laser-nanowire interaction. To provide insight into the radiative processes, we plot the spatial distribution of the averaged (over the local electron distribution) radiated power density in Figs. 4(a-c) and of the averaged electron quantum parameter, χ_e in Figs. 5(a-c), at the same times as in Figs. 2(a-c). We remind that the power radiated by a single electron can be expressed as $P = (2/3) \alpha_f m_e c^2 \chi_e^2 g(\chi_e) / \tau_C$, with $\tau_C = \hbar / m_e c^2$ the Compton time, α_f the fine structure constant, and $g(\chi_e)$ a quantum correction [25]. The scaling $P \propto \chi_e^2$ is a good approximation in the classical regime ($\chi_e \lesssim 0.05$). These maps will help analyze the time evolution of the angle-resolved radiated power and the photon energy spectra (integrated over different time intervals) plotted in Figs. 6(a,b). The angle θ_γ denotes the angle of the photon momentum \mathbf{k}_γ relative to the laser axis (x), *i.e.*, $\theta_\gamma = \arccos(k_{\gamma,x}/k_\gamma) \in (0, \pi)$.

Figure 6(a) indicates that the emission initially occurs in the laser direction ($\theta_\gamma = 0$) with an increasingly broad angular distribution. As expected, the emission strongly increases at the laser peak, and is at its brightest in the time period $5 \lesssim t \lesssim 20$ fs. Figure 6(b) shows that the spectrum radiated from the start of the interaction up to $t = +25$ fs extends to $\hbar\omega_{\text{max}} \simeq 60$ MeV, and makes up $\sim 40\%$ of the total radiated energy. The radiated power is then contained in a forward cone of $\sim 45^\circ$ half angle and is modulated at twice the laser frequency. This oscillation is typical of the synchrotron radiation from a relativistically overdense plasma layer in the SDE

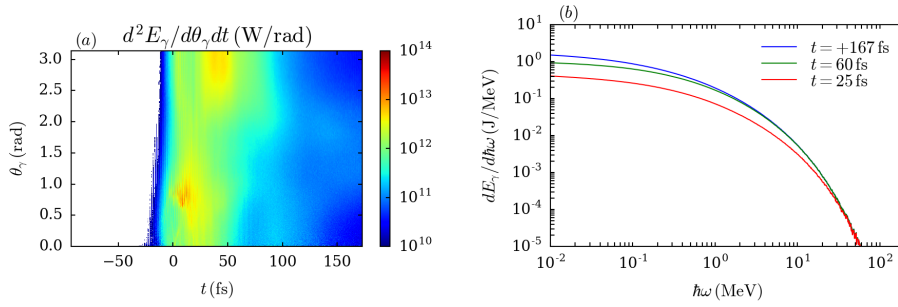


Figure 6. (a) Time evolution of the angle-resolved radiated power and (b) photon energy spectra integrated from the start of the interaction up to three different times: $t = +25$ fs (red curve), $+60$ fs (green curve) and $+167$ fs (blue curve). Angles in (a) are defined as $\theta_\gamma = \arccos(k_{\gamma,x}/k_\gamma) \in (0, \pi)$.

regime [75]. Consistently, Fig. 4(a), recorded at $t = +8$ fs, shows that the emission then mainly occurs at the front side of the plasma (with electron density $n_e \simeq 10 - 50n_c$) filling the wire gaps, where relatively high values $\chi_e \simeq 5 \times 10^{-2} - 10^{-1}$ are found. Deeper into the array ($15 \leq x \leq 20 \mu\text{m}$), the more dilute, λ_0 -periodic electron bunches that move along the laser wave present a weaker quantum parameter, $\chi_e < 10^{-2}$ (due to compensating electric and magnetic forces), and hence emit little energy. Note, however, the relatively bright synchrotron spots at the right-hand tips of the wires, where space-charge fields deflect the electrons at an angle to the laser direction, hence increasing their quantum parameter (see below).

Figure 6(a) reveals that a secondary emission burst occurs in the time interval $25 \lesssim t \lesssim 60$ fs, when the transmitted laser pulse travels across the target backside. In contrast to the first emission burst, this emission takes place in the backward direction ($\theta_\gamma \simeq \pi$). It originates from the interaction of the transmitted part of the laser pulse with the fast electrons reflected at the target backside by the space-charge field. Such a counterpropagating geometry maximizes the quantum parameter $\chi_e \simeq 2\gamma E_\perp/E_S$ (where E_\perp is the laser electric field). This mechanism is supported by Fig. 4(b), which shows a volumetric emission between (and near the backside of) the wires, where χ_e values of $\sim 10^{-2}$ are reached [Fig. 5(b)]. About 45% of the synchrotron yield is radiated during this stage (with maximum photon energies ~ 60 MeV, similar to those in the primary stage). Of course, this phenomenon will be altered in the presence of a substrate coated at the target backside (see Sec. 3). We note that relatively high χ_e values ($\sim 10^{-2}$) are also reached in the dilute plasma formed in front of the target, yet the electron density, $n_e \simeq 0.1n_c$ [Fig 3(b)] is there too low to yield significant emission.

Following the laser irradiation ($t \gtrsim 60$ fs), the radiated power strongly drops, yet, in similar fashion to Ref. [48], the remaining magnetostatic fields can sustain additional radiation [Fig. 6(a)]. Figure 5(c) thus indicates that, at $t = +167$ fs, χ_e attains values $\sim 10^{-3}$ in the magnetic modulations. The weaker power radiated at such low χ_e values [Fig. 4(c)] is partially compensated for by the longer duration of this emission stage, which makes up $\sim 15\%$ of the total yield in the time period $60 \lesssim t \lesssim 167$ fs [Fig. 6(b)]. Since the magnetostatic fields build up early in the laser irradiation, their contribution is *a priori* not limited to the final times of the simulation. Yet their effect is initially mitigated by the transverse electrostatic field ($\langle E_y \rangle$) around the

wires, which tends to weaken the quantum parameter; as the wires radially expand and mix [Fig. 3(c)], however, $\langle E_y \rangle$ diminishes and becomes small compared to $\langle B_z \rangle$, so that $\chi_e \simeq \langle \gamma \rangle \langle B_z \rangle c / E_S$. At $t = 167$ fs, we have $\langle B_z \rangle \simeq 15B_0$ and a mean electron energy $\langle \gamma_e \rangle \simeq 23$ in the expanded plasma, which implies $\chi_e \simeq 8 \times 10^{-4}$, consistent with Fig. 5(c).

Our reference simulation has allowed us to pinpoint important processes affecting the synchrotron radiation in the interaction of a 10^{22} Wcm^{-2} femtosecond laser pulse with a nanowire array of micron-scale interspacing. We will now examine the dependencies of the emission on the wire and laser parameters.

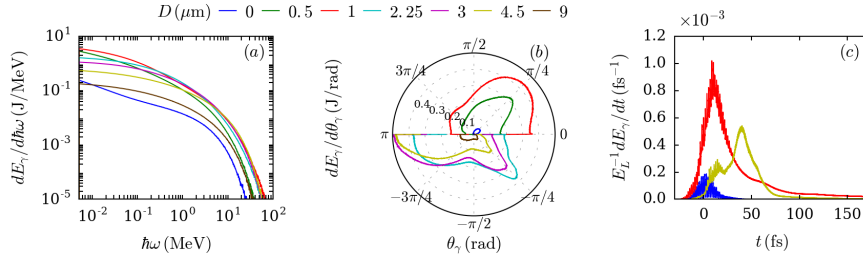


Figure 7. Variations of the synchrotron emission with the interwire spacing D : (a) energy spectra, (b) angle-resolved radiated energy and (c) time-resolved radiated power (and normalized to the total laser energy E_L). Each color represents a different value of D (in μm units) as indicated in the legend of panel (a). Angles in (b) are defined as $\theta_\gamma = \arccos(k_{\gamma,x}/k_\gamma) \in (0, \pi)$ and the resulting angular distribution is symmetrized with respect to $\theta_\gamma = 0$. All plotted quantities are integrated over the simulation domain.

2. Parametric scan on the nanowire parameters and the laser intensity

In the following, we explore the dependency of the angle-energy spectra of the synchrotron radiation on the nanowire spacing (D), width (d) and material (Z), as well as on the laser intensity (I). Except for the varied parameter, the numerical setup is identical to that presented in Sec. 1.1. Our parametric scan will encompass various regimes of synchrotron radiation, which will be interpreted in light of the processes revealed in the reference case of Sec. 1.2 and previous simulation works [71, 46, 55, 56].

2.1. Variation of the interwire spacing: from forward to backward directed radiation

In our simulations, the interwire spacing has been varied over the set of values $D \in [0, 0.5, 1, 2.25, 3, 4.5, 9] \mu\text{m}$. Note that $D = 0 \mu\text{m}$ corresponds to a planar target. The chosen values exactly divide the transverse size of the domain ($L_y = 9 \mu\text{m}$) so as to keep the periodic condition valid. The other target parameters are set to $d = 0.3 \mu\text{m}$, $L = 10 \mu\text{m}$, $Z = 6$ and the laser intensity is $I = 10^{22} \text{Wcm}^{-2}$.

The energy-resolved photon spectra recorded for various interwire spacings are plotted in Fig. 7(a). We see that the cutoff photon energy weakly varies for $1 \leq D \leq 4.5 \mu\text{m}$, where it reaches a maximum value $\hbar\omega_{\text{max}} \simeq 50 \text{MeV}$, approximately twice that found at uniform density ($\simeq 23 \text{MeV}$). Figure 7(b), which displays the angle-resolved energy spectra, shows a transition from a mainly forward-directed emission at $D \leq 1 \mu\text{m}$ to an increasingly backward-directed emission at larger spacings. The two lobes of emission found at $D \geq 2.25 \mu\text{m}$ around the directions $\theta_\gamma \simeq 45^\circ$ and $\theta \simeq 180^\circ$ originate from the same mechanisms discussed in Sec. 1.2. In particular, we emphasize that the backward emission follows from the electrons refluxing in the $-x$ direction and colliding head-on with the transmitted part of the laser pulse. This results in a secondary backward-directed γ -ray burst after the primary (and weaker) forward-directed burst. This is evidenced in Fig. 7(c) where is plotted the time evolution of the radiated power: the curve at $D = 4.5 \mu\text{m}$ presents two distinct emission peaks, the second, brighter one taking place at $t \simeq 40 \text{fs}$, *i.e.*, as the laser pulse exits the target.

At narrower spacings ($D \leq 1 \mu\text{m}$), the interstices fill up with opaque plasma

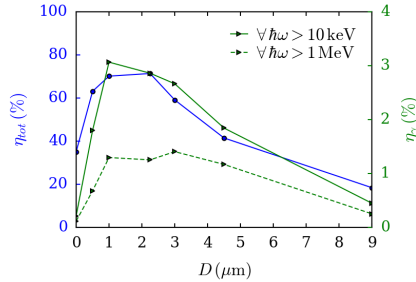


Figure 8. Variations with the interwire spacing (D) of the total absorbed laser energy fraction (η_{tot} , blue circles) and radiation conversion efficiency (η_γ , green triangles). The radiation conversion efficiency is computed for two photon energy thresholds: $\hbar\omega \geq 10$ keV (green solid) and $\hbar\omega \geq 1$ MeV (green dashed). All quantities are integrated over the simulation duration.

increasingly early before the laser pulse maximum. Looking at the increase in the instantaneous laser reflectivity, we find that the transparency-opacity transition occurs at $\tau_f \simeq -8$ fs for $D = 0.5 \mu\text{m}$ and $\tau_f \simeq 3$ fs for $D = 1 \mu\text{m}$. The energy fraction and mean intensity of the transmitted light then diminishes with decreasing D , which greatly weakens the aforementioned backward emission mechanism. At $D = 2.25 \mu\text{m}$, about 13 % of the laser energy is transmitted, and this fraction becomes negligible for $D \leq 1 \mu\text{m}$. The time history of the radiated power at $D = 1 \mu\text{m}$, plotted in Fig. 7(c), thus presents a single maximum, occurring at $t \simeq 10$ fs, just after the overdense plasma filling of the vacuum gaps. The primary radiation burst observed at $D = 4.5 \mu\text{m}$ occurs approximately at the same time: both signals exhibit a $2\omega_0$ modulation, characteristic of SDE in an overcritical plasma [75]. The photons are then emitted in a large forward cone, as seen in the upper part of Fig. 7(b).

As pointed out in the Introduction, the interest for nanowire targets as potentially efficient radiation sources arose from their well-established capability in yielding high laser absorption fractions. Since the latter usually translate in large numbers of energetic electrons, it is tempting to predict that the laser absorption and radiation yield are correlated. To check this scenario, we plot in Fig. 8 the variations of the total absorbed laser energy fraction (η_{tot} , defined as the energy absorbed by all the particle and photon species, normalized to the laser energy) and the laser-to-photon energy conversion efficiency (η_γ) with the interwire spacing. To discriminate between the contributions of the ‘low’ and ‘high’ energy photons in the radiation yield, the green solid and dashed η_γ curves are computed applying lower-energy cutoffs $\hbar\omega = 10$ keV and 1 MeV, respectively. We note that the laser absorption rises from $\sim 35\%$ at uniform solid density to $\sim 70\%$ at $D = 2.25 \mu\text{m}$, with a plateau above $\sim 60\%$ in the range $1 \leq D \leq 3 \mu\text{m}$. While the η_{tot} and η_γ curves look similar, a few quantitative differences are discernible. Both η_γ curves starting from very low values ($\sim 0.2\%$ for $\hbar\omega \geq 10$ keV and $\sim 0.1\%$ for $\hbar\omega \geq 1$ MeV) at uniform solid density, they present a steeper rise at low D values ($\leq 1 \mu\text{m}$) than η_{tot} . Also, η_γ attains its maximum ($\sim 3\%$, for $\hbar\omega \geq 10$ keV) at $D = 1 \mu\text{m}$, lower than the value optimizing η_γ . For $\hbar\omega \geq 1$ MeV, we find $\eta_\gamma \simeq 1\%$ in a broader range of interwire spacings, $1 \leq D \leq 4.5 \mu\text{m}$, with a weakly pronounced optimum at $D = 3 \mu\text{m}$.

The overall evolution of the total laser absorption, as depicted in Fig. 8, is

consistent with the results obtained in Ref. [71] at lower laser intensity ($I = 5 \times 10^{19} \text{ W/cm}^2$) and in the sub-micron range $0.24 \leq D \leq 0.8 \mu\text{m}$ (with $d = 0.16 \mu\text{m}$). In our work, by considering larger interwire spacings, we allow greater fractions of the laser light to be transmitted through the target, thus enabling the secondary radiation burst at the target backside discussed above. Moreover, in the laser intensity range $10^{18} - 10^{21} \text{ Wcm}^{-2}$, it is commonly believed that increasing the wire spacing enables the electrons to reach higher energies [76, 56, 70]. Our results partially corroborate this behavior at $I = 10^{22} \text{ Wcm}^{-2}$: the mean energy of the electrons above 511 keV is found to increase from $\langle E_e \rangle = m_e c^2 \langle \gamma \rangle \simeq 5 \text{ MeV}$ at $D = 0$ to $\langle E_e \rangle \simeq 15 \text{ MeV}$ at $D = 2.25 \mu\text{m}$. At larger spacings, $2.25 \leq D \leq 9 \mu\text{m}$, the mean hot-electron energy is found to saturate at $\langle E_e \rangle \simeq 20 \text{ MeV}$, relatively close to the ponderomotive scaling $\langle E_e \rangle \simeq m_e c^2 \left(\sqrt{1 + a_0^2/2} - 1 \right) \simeq 30 \text{ MeV}$ [77, 78].

To summarize, we have identified two distinct regimes of synchrotron radiation by varying the interwire spacing. For narrowly spaced wires ($D \leq 1 \mu\text{m}$), the vacuum gaps rapidly fill up with overdense plasma before the on-target laser peak, causing the emission to be concentrated at the target front and mainly forward directed, similarly to what occurs in a uniform overdense plasma. At larger interwire spacings ($D \geq 2.25 \mu\text{m}$), this mechanism is progressively superseded by an additional emission taking place at the target backside, which results from the interaction of the transmitted laser light with the refluxing fast electrons. This backward-directed emission is distinct from the RESE mechanism highlighted in Ref. [46], which occurs at the moving laser front in relativistically underdense plasmas. To achieve the dilute plasma conditions required by the latter mechanism during the laser pulse, the wire width must be reduced, as is done in the next Section.

2.2. Variation of the wire width: from RESE to SDE, through TOEE

We now set the interwire spacing to the value maximizing the radiation efficiency, $D = 1 \mu\text{m}$, and vary the wire width in the set of values $d \in (15, 36, 50, 100, 300, 500, 1000) \text{ nm}$. Note that the value $d = 1 \mu\text{m}$ corresponds to a uniform solid-density target. The resulting energy-angle photon spectra and radiation dynamics are displayed in Fig. 9(a-c).

For $d \lesssim \delta_{acc} \simeq 30 \text{ nm}$, most of the electrons are expelled from the wires by the laser field, hence leading to fast (*i.e.*, before ion expansion) homogenization of the plasma profile at the average density $n_{av} = n_e d/D$. For $d = 15 \text{ nm}$, one has $n_{av} \simeq 7n_c$, which falls into the regime of relativistic self-induced transparency (RSIT). Such plasma conditions have been shown to favor the RESE process [46]: the electrons, pushed by the ponderomotive force at the laser front, are periodically reinjected back into the laser wave by the charge separation field. Their momentum ($\sim a_0 m_e c$) then forms an angle of $\sim \pi$ with the laser wavevector, which maximizes the quantum parameter $\chi_e \sim 2a_0^2 c B_0 / E_S \sim 5 \times 10^{-6} a_0^2$ and the subsequent synchrotron radiation in the backward direction. Figure 9(b) confirms this prediction, showing that practically all the radiation is then directed backwards. In Fig. 9(c), we observe a temporal modulation of the radiated power at a period of $\sim 15 \text{ fs}$, of the same order as the theoretical estimate $\tau_{RESE} = a_0 / (n_e \omega_0) \simeq 7 \text{ fs}$ derived for RESE in uniform plasmas [46]. This period is significantly larger than that of the $2\omega_0$ oscillations arising in the SDE regime (see the curve with $d = 500 \text{ nm}$, corresponding to $n_{av} = 240n_c$).

As discussed below [see Fig. 15(a) in Sec. 2.4], we have checked the occurrence

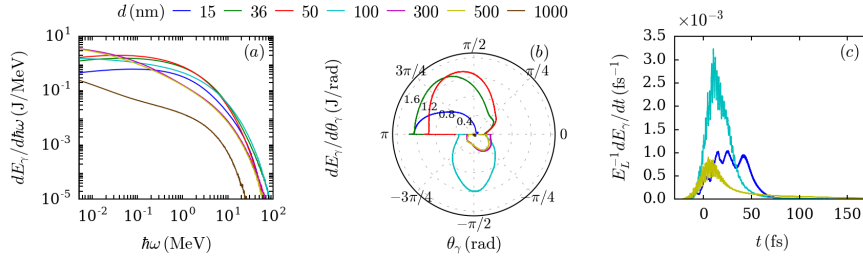


Figure 9. Variations of the synchrotron emission with the wire width d : (a) energy spectra, (b) angle-resolved radiated energy and (c) time-resolved radiated power (normalized to the total laser energy E_L). Each color represents a different value of d (in nm units) as indicated in the legend of panel (a). Angles in (b) are defined as $\theta_\gamma = \arccos(k_{\gamma,x}/k_\gamma) \in (0, \pi)$ and the resulting angular distribution is then symmetrized with respect to $\theta_\gamma = 0$. All plotted quantities are integrated over the simulation domain.

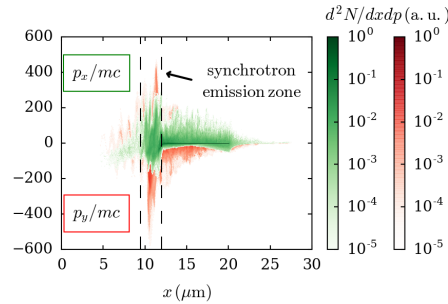


Figure 10. Electron $x - p_x$ (green colormap) and $x - p_y$ (red colormap) phase spaces at $t = +40$ fs. The nanowire-array parameters are $d = 100$ nm, $D = 1 \mu\text{m}$ and $L = 10 \mu\text{m}$, giving rise to transversally oscillating electron synchrotron emission (TOEE).

of RSIT by measuring the effective propagation velocity of the laser front in the homogenized plasma, in similar fashion to Ref. [79]. RSIT is found to occur for $d \lesssim 50 - 100$ nm, thus leading to significant laser transmission across the plasma. For wire widths $\gtrsim 100$ nm, the homogenized plasma becomes opaque to the laser light, which then propagates at a much reduced speed through hole boring (HB) [79].

The synchrotron spectra of Fig. 9(a) show that the maximum photon energy weakly varies ($\hbar\omega_{\text{max}} \simeq 50 - 70$ MeV), and in a non-monotonic way, for $15 \leq d \leq 300$ nm. The most notable variation occurs when the wire width is increased from $d = 300$ nm to $d = 500$ nm, leading to $\hbar\omega_{\text{max}}$ decreasing from ~ 50 MeV to ~ 20 MeV. More interestingly, it is found that the mean photon energy is maximized in the RSIT regime: for $d = 15$ nm, we obtain $\langle \hbar\omega \rangle \simeq 0.45$ MeV, much higher than for $d \geq 300$ nm, which leads to a relativistically overdense homogenized plasma ($n_{av} = 144n_c$) and $\langle \hbar\omega \rangle \simeq 0.14$ MeV.

The case of $d = 100$ nm, close to the RSIT/HB threshold, yields the highest maximum photon energies [Fig. 9(a)] but also, and more significantly, to a radiated energy concentrated in the transverse direction, $\theta_\gamma = \pi/2$ [Fig. 9(b)]. This particular

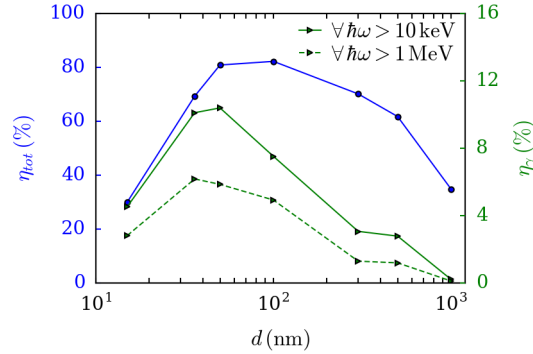


Figure 11. Variations with the wire width (d) of the total absorbed laser energy fraction (η_{tot} , blue circles) and radiation conversion efficiency (η_γ , green triangles). The radiation conversion efficiency is computed for two photon energy thresholds: $\hbar\omega \geq 10 \text{ keV}$ (green solid) and $\hbar\omega \geq 1 \text{ MeV}$ (green dashed). All quantities are integrated over the whole simulation duration.

radiation pattern corresponds to the TOEE regime evidenced in Ref. [45]. In this mechanism, a balance is established between the laser ponderomotive force and the charge-separation field at the irradiated plasma front. This causes the electrons to predominantly oscillate in the transverse plane, thus inducing a mainly transverse synchrotron emission. This particular electron dynamics stands out in Fig. 10, which superimposes the $x - p_x$ (green colormap) and $x - p_y$ (red colormap) electron phase spaces at $t = +40 \text{ fs}$. Around the front side of the target where most of the radiation is emitted, the electron distribution is clearly more extended in the transverse direction than in the longitudinal direction. As the wire width is decreased (resp. increased) from $d \simeq 100 \text{ nm}$, the radiation pattern is shifted to the backward (resp. forward) direction, characteristic of the RESE (resp. SDE) mechanism.

Figure 11 displays the wire-width dependence of the total laser absorption (η_{tot}) and radiation conversion efficiencies (η_γ) into $> 10 \text{ keV}$ and $> 1 \text{ MeV}$ energy photons. The laser absorption rises from $\eta_{tot} \sim 30 \%$ at $d = 15 \text{ nm}$ to a maximum of $\sim 80 \%$ at $d = 50 - 100 \text{ nm}$, before dropping to $\sim 35 \%$ in the uniform-density case ($d = 1 \mu\text{m}$). While the increase in η_{tot} at low wire widths is accompanied by similar rises in the η_γ curves, the latter attain their maxima (at $d \simeq 36 - 50 \text{ nm}$) slightly before η_{tot} . A peak value of $\eta_\gamma \sim 10.4 \%$ (resp. 6.1%) for $\hbar\omega \geq 10 \text{ keV}$ (resp. $> 1 \text{ MeV}$) is obtained at $d = 50 \text{ nm}$ (resp. $d = 36 \text{ nm}$). Moreover, the two η_γ curves show a faster decrease at large d than η_{tot} . To quantify this, let us compare the cases of $d = 36 \text{ nm}$ and $d = 300 \text{ nm}$: although both widths give rise to similar absorption fractions ($\eta \simeq 70 \%$), the photon yield at $d = 36 \text{ nm}$ is ~ 3 times larger than at $d = 300 \text{ nm}$. This marked difference follows from the distinct plasmas produced by the electron-depleted exploding wires: at $d = 36 \text{ nm}$, a relativistically undercritical plasma ($n_{av} = 17n_c$) forms, which triggers a RESE-type mechanism more efficient than SDE that arises in the overcritical plasma ($n_{av} = 144n_c$) generated at $d = 300 \text{ nm}$. Finally, we note that at $d = 15 \text{ nm}$, a sizable fraction ($\sim 70 \%$) of the laser energy is transmitted across the array, which mechanically reduces the radiated energy fraction.

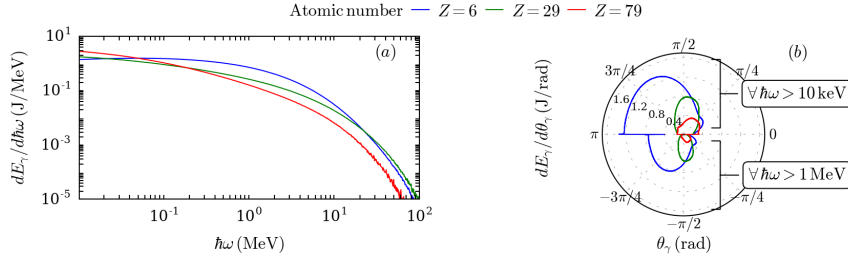


Figure 12. Wire-material dependence of the (a) energy-resolved and (b) angle-resolved radiated energy. The blue, green and red curves correspond, respectively, to C, Cu and Au wires. The top (resp. bottom) half of panel (b) is associated with a photon energy threshold of 10 keV (resp. 1 MeV). All spectra are integrated over the simulation duration. Angles in (b) are defined as $\theta_{\gamma} = \arccos(k_{\gamma,x}/k_{\gamma}) \in (0, \pi)$, and the resulting angular distribution is symmetrized with respect to $\theta_{\gamma} = 0$.

2.3. Changing the ion mass and the laser intensity

We now demonstrate that modifying other key parameters of the interaction such as the wire material or the laser intensity can also enable switching between the previously discussed radiation mechanisms. To this goal, we first replace, in the most efficient configuration for γ -ray production ($D = 1 \mu\text{m}$, $d = 36 \text{ nm}$), the neutral carbon atoms ($Z = 6$) by either copper ions ($Z = 29$) with a 5+ initial ionization degree and a solid density $n_{Cu} = 80n_c$, or gold ions ($Z = 79$) with a 14+ initial ionization degree and a solid density $n_{Au} = 55n_c$. Second, we vary the laser intensity in the range $I = 10^{21} - 10^{23} \text{ Wcm}^{-2}$ for two values of the wire widths: $d = 100 \text{ nm}$ and $d = 300 \text{ nm}$.

The energy-resolved radiated energy displayed in Fig. 12(a) indicates that the average photon energy is decreased by the use of copper (0.27 MeV) and gold (0.14 MeV) compared to carbon (0.41 MeV). The radiation efficiency above 10 keV also drops with increasing atomic number (from $\sim 10.1\%$ in carbon to 4.6% in copper and 2.9% in gold), in spite of a slightly enhanced laser absorption in copper and gold ($\eta_{tot} \sim 80\%$) than in carbon ($\sim 70\%$, see Fig. 11). In light of our previous results, the reason for this difference is that the homogenized electron density ($n_{av} = 17n_c$) in the carbon wires lies in the RSIT regime, prone to RESE. In contrast, the copper (resp. gold) wires produce a higher-density plasma, $n_{av} = 80n_c$ (resp. $n_{av} = 3000n_c$), opaque to the laser field, which favours TOEE (resp. SDE). This transition from RESE to SDE through TOEE is supported by the angular radiation patterns shown in Fig. 12(b): both for the 10 keV and 1 MeV photon energy thresholds, we clearly see that the emission evolves from a mainly backward radiation in the carbon target to a predominately transverse radiation in copper and to a forward directed radiation in gold.

In the gold case, we observe ionization rates up to $Z^* = 70$ at the laser-target interface, consistent with Ref. [67] where a similar setup is numerically considered. Also, the synchrotron photon yield above 1 MeV ($\sim 1.9\%$) is about 60% of the yield above 10 keV, similarly to the carbon and copper targets. Although this performance is not optimal due to too dense a homogenized plasma, it can be put in perspective with

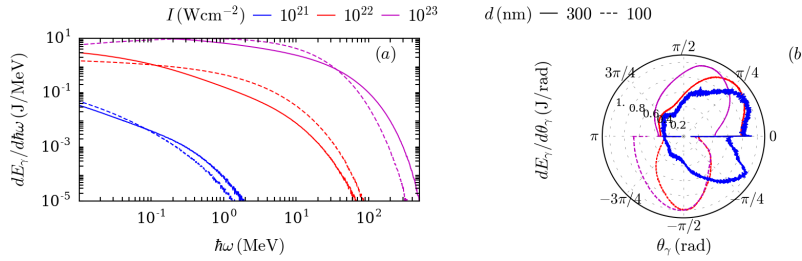


Figure 13. Laser-intensity dependence of (a) the energy-resolved and (b) angle-resolved radiated energy (above 10 keV). Each color stands for a particular value of I as indicated in the legend. The solid (resp. dashed) curves correspond to a wire width $d = 300$ nm (resp. 100 nm). The interwire spacing is set to $D = 1 \mu\text{m}$. Angles in (b) are defined as $\theta_{\gamma} = \arccos(k_{\gamma,x}/k_{\gamma}) \in (0, \pi)$, and the resulting angular distribution is symmetrized with respect to $\theta_{\gamma} = 0$.

the record $\sim 20\%$ conversion efficiency into > 1 keV photons which has been recently reported using gold nanowires driven by a $4 \times 10^{19} \text{ Wcm}^{-2}$, 55 fs laser pulse [62]. Rather than synchrotron emission, x-ray radiation in this experiment is caused by atomic physics processes (atomic line emissions, photorecombination and Bremsstrahlung). Another difference with our study is that, due to lower laser intensity, and hence slower nanowire expansion, the highest x-ray yield is found for significantly smaller interspacings ($\sim 0.1 \mu\text{m}$). The measured x-ray yield, however, rapidly drops with increasing photon energies (below 1% for $\hbar\omega > 6$ keV). These results should stimulate further theoretical work on the radiation efficiencies of atomic physics and synchrotron processes as functions of the laser and nanowire parameters.

We now return to carbon nanowires and examine the photon distributions produced in the laser intensity range $10^{21} \leq I \leq 10^{23} \text{ Wcm}^{-2}$. Figure 13(a) reveals that the photon generation at $I = 10^{21} \text{ Wcm}^{-2}$ occurs with the same efficiency for the two chosen values of the wire width, $d = 100$ nm (dashed lines $\eta_{\gamma} \simeq 0.09\%$) and $d = 300$ nm (solid lines $\eta_{\gamma} \simeq 0.08\%$). The case of $d = 300$ nm, however, leads to higher maximum ($\hbar\omega_{\text{max}} = 1.4 \rightarrow 1.8 \text{ MeV}$) and average ($\langle \hbar\omega \rangle = 32 \rightarrow 42 \text{ keV}$) photon energies. At higher intensity ($I \geq 10^{22} \text{ Wcm}^{-2}$), by contrast, the average photon energy is much larger at $d = 100$ nm than at $d = 300$ nm (400 keV *vs.* 140 keV). This stems from the fact that the expanded plasma then becomes relativistically transparent, whereas it remains opaque at $d = 300$ nm (even at $I = 10^{23} \text{ Wcm}^{-2}$). Furthermore, the fraction of laser energy converted into ≥ 10 keV photons is always higher at $d = 100$ nm whatever the laser intensity in the studied range.

In Fig. 13(b), it is seen that the emission cone angle increases with increasing laser intensity. While at $d = 300$ nm the radiation remains forward-directed up to $I = 10^{23} \text{ Wcm}^{-2}$, at $d = 100$ nm it is forward directed at $I = 10^{21} \text{ Wcm}^{-2}$, becomes concentrated in the transverse direction at $I = 10^{22} \text{ Wcm}^{-2}$, and is mainly confined within angles $\geq \pi/2$ at $I = 10^{23} \text{ Wcm}^{-2}$. Once again we stress that this evolution from SDE to RESE results from the onset of RSIT at high enough laser intensity. In the latter case, the radiation is mostly carried by γ -ray photons: the radiation conversion efficiency above 1 MeV indeed reaches $\sim 43\%$, hardly lower than the $\sim 47\%$ conversion fraction in ≥ 10 keV photons.

Since the radiation power should scale approximately as χ_e^2 , it is worthwhile to

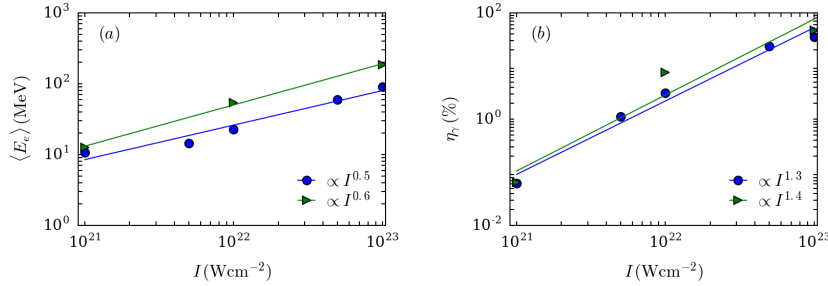


Figure 14. (a) Hot-electron (> 0.511 MeV) mean energy and (b) radiation conversion efficiency into > 10 keV photons as a function of the laser intensity. The green triangles (resp. blue circles) correspond to a wire width $d = 100$ nm (resp. 300 nm). The interwire spacing is set to $D = 1 \mu\text{m}$.

inspect the variations of the mean hot-electron energy $\langle E_e \rangle$ (counting all electrons above 0.511 MeV) as a function of the laser intensity. Figure 14(a) plots $\langle E_e \rangle$ for the wire widths $d = 100$ nm (green triangles) and $d = 300$ nm (blue circles). Both curves are consistent with an approximate scaling $\langle E_e \rangle \propto I^{0.5-0.6}$, quite close to the fit $\langle E_e \rangle \propto I^{0.4}$, reported at lower intensities ($10^{18} \leq I \leq 3 \times 10^{20} \text{ Wcm}^{-2}$) in Ref. [72]. The fact that $\langle E_e \rangle$ roughly obeys the well-known ponderomotive law [77] is not *a priori* obvious given the various heating mechanisms possibly at play in the nanowire array: from Brunel-type acceleration at the wire walls to stochastic heating in the interference field pattern inside the vacuum gaps, and ponderomotive acceleration in the homogenized plasma. It should be noted that the acceleration of super-ponderomotive electrons was recently demonstrated in the case of a nanowire array with $d = 1.5 \mu\text{m}$ and $D = 7 \mu\text{m}$, driven at $I \simeq 10^{21} \text{ Wcm}^{-2}$ [76]. The main difference between this work and ours is the plasma-filling time of the interstices: the large interspacing in the experiment allows the laser to efficiently propagate between the wires, and energize electrons via the so-called direct laser acceleration mechanism [76]. In our case, such an efficient laser penetration is hampered by the fast homogenization of the nanostructure front, due to the comparatively lower interspacing $D = 1 \mu\text{m}$ investigated (at $I = 10^{21} \text{ W/cm}^2$, the fraction of energy transmitted across the target is $< 1\%$).

In Fig. 14(b) is plotted the radiation conversion efficiency (counting all photons above 10 keV) as a function of the laser intensity. The results can be approximately fitted to $\eta_\gamma \propto I^{1.3-1.4}$. This scaling happens to fall in between the one found at undercritical densities in the RESE regime, $\eta_\gamma \propto I$ [46], and the one observed at overcritical densities in the SDE regime, $\eta_\gamma \propto I^{3/2}$ [80]. This behavior could be expected since both radiation regimes can arise in our broad intensity range. Regarding the radiation efficiency, these two mechanisms mainly differ in the typical number of radiating electrons (N_e). In the underdense plasma, this number is proportional to the areal density crossed by the laser, $N_e \propto n_e$; in an overdense plasma, this number scales as the areal density of the compressed electron layer at the target front, $N_e \propto I^{1/2}$. Since $\eta_\gamma \propto N_e \chi_e^2 / I$ and $\chi_e \propto I$, we thus expect $\eta_\gamma \propto I$ for RESE and $\eta_\gamma \propto I^{3/2}$ for SDE.

2.4. Comparison with uniform-density targets

The dominant radiation processes that we have highlighted in nanowire arrays appear similar to those identified in previous simulation studies considering uniform plasmas. This is so because, under the present interaction conditions, the nanostructure is largely smoothed out during the laser pulse, so that a large part of it experiences a significantly homogenized plasma. One may then question the advantage, regarding synchrotron radiation, of using nanowire arrays compared to uniform plasmas at sub-solid densities. To answer this question, we have conducted a set of simulations considering a $10\ \mu\text{m}$ -thick carbon layer of uniform (free electron) density varying from $Zn_i = 7n_c$ to $480n_c$ (solid density). This density range corresponds to that achieved in fully homogenized nanowire arrays ($n_{av} = Zn_C d/D$) when increasing the wire width from $d = 15\ \text{nm}$ to $1\ \mu\text{m}$ at fixed spacing $D = 1\ \mu\text{m}$. The laser intensity is set to $I = 10^{22}\ \text{Wcm}^{-2}$.

First, we examine the transition between plasma transparency (RSIT) and opacity (HB), which appears critical in determining the properties of the synchrotron emission. To properly identify the regime of laser-plasma interaction, we have tracked the position of the laser front in the target, $x_f(t)$, defined such that $a(x_f(t), t) = \max_x a(x, t)/2$, with $a(x, t)$ being the y -averaged dimensionless laser field. This definition is similar to that used in Ref. [79] except that, due to our short pulse duration, we use $\max_x a(x, t)/2$ instead of $a_0/2$ as is relevant to a semi-infinite pulse. For each simulation, v_f is evaluated from a linear regression fit of $x_f(t)$. Figure 15(a) plots v_f as a function of the wire width (d) in the nanowire-array case, and of the electron density ($n_e \equiv n_{av}$) in the uniform-plasma case. Both target types lead to a similarly decreasing curve for v_f , which drops from $v_f/c \simeq 0.7$ at $n_{av} = 7n_c$ down to $v_f/c \simeq 0.2$ at $n_{av} = 32n_c$. This parameter range corresponds to RSIT, and we have further checked that the laser wave then overlaps with the plasma electrons and ions, as expected [81]. Nanowire arrays tend to yield slightly faster laser propagation, which is ascribed to inhomogeneity effects. For completeness, we have plotted (as a black solid line) the front velocity estimated in Ref. [79] in a simpler setting (1D geometry, semi-infinite pulse, no synchrotron losses), $v_{RSIT}/c \simeq \exp(-2n_{av}/n_{cr})\sqrt{1 - n_{av}/n_{cr}}$, where $n_{cr} \simeq 0.89a_0n_c$ in the ultrarelativistic regime. Despite the short duration and time-varying intensity of our laser pulse, correct agreement is found between v_f and v_{RSIT} up to $n_{av} \simeq 48n_c$ (or $d \simeq 100\ \text{nm}$), where the transition from RSIT to HB occurs, also corresponding to the transition threshold between RESE and SDE [see Figs. 9(b) and 10]. At higher n_{av} or d , the front velocity approximately matches the theoretical HB velocity (black dashed line), $v_{HB}/c \simeq \Pi/(1 + \Pi)$, where $\Pi = \sqrt{IZ/Am_e n_{av} c^3}$ [79].

In Fig. 15(b) are plotted the absorbed and transmitted laser energy fractions as functions of the wire width (d) in the nanowire-array case, and of the plasma density ($n_e \equiv n_{av}$) in the uniform-target case. Similarly, Fig. 15(c) plots, for both target types, the variations with n_{av} and d of the conversion efficiencies into $> 10\ \text{keV}$ and $> 1\ \text{MeV}$ photons. In uniform targets, the laser absorption strongly increases (from $\eta_{tot} \sim 35\%$ to $\sim 75\%$) with increasing density in the range $7 \leq n_{av} \leq 24n_c$. Similar variations are found in nanowire arrays with same equivalent density (*i.e.*, $15 \leq d \leq 50\ \text{nm}$), with the differences, however, that η_{tot} is a bit smaller ($\sim 30\%$) at $n_{av} = 7n_c$, but larger ($\sim 80\%$) at $n_{av} = 24n_c$. In this parameter range, the interaction takes place in the RSIT regime in both targets, yet the transmitted laser fraction is always a bit larger in nanowire arrays, reaching $\sim 70\%$ at $n_{av} = 7n_c$ and $\sim 10\%$ at $n_{av} = 24n_c$. The most pronounced difference between the two target types arises at larger n_{av} or

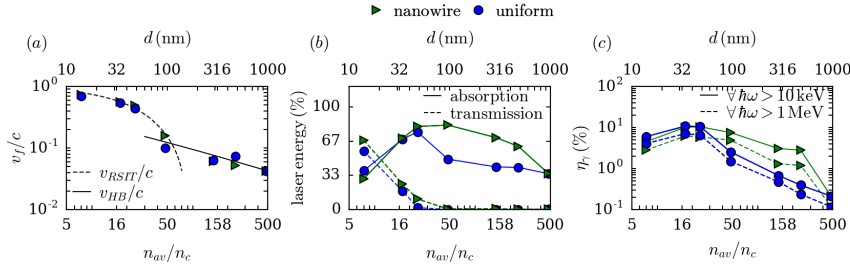


Figure 15. Comparison between carbon nanowire arrays (green triangles) and uniform-density targets (blue circles): (a) propagation velocity of the laser front; (b) total laser absorption (solid lines) and transmission (dashed lines); (c) radiative conversion efficiencies into > 10 keV (solid lines) and > 1 MeV photons (dashed lines). Results from nanowire-array (resp. uniform-density) targets are plotted as functions of the wire width d (resp. the average electron density n_{av}). In (a), the black solid and dashed lines plot the theoretical front velocities v_{RST} and v_{HB} , respectively (see text). In (b) and (c), all quantities are integrated over the simulation duration.

d : while the laser absorption in uniform targets abruptly drops beyond $n_{av} = 24n_c$, (down to $\eta_{tot} \simeq 45\%$ at $n_{av} = 64n_c$, and $\eta_{tot} \simeq 35\%$ at solid density), it stays at a high level ($\gtrsim 70\%$) up to $n_{av} = 144n_c$ (i.e., $d = 300$ nm).

The general trends observed for the laser absorption also hold for the synchrotron radiation. While uniform targets yield slightly better radiation efficiencies at $n_{av} = 7n_c$ ($\eta_\gamma \simeq 6\%$ vs. $\sim 4.5\%$, for $\hbar\omega > 10$ keV), both setups give very similar maximum efficiencies, $\eta_\gamma \simeq 10\%$ (resp. $\sim 6\%$) for $\hbar\omega > 10$ keV (resp. > 1 MeV) in the range $n_{av} = 17 - 24n_c$ (i.e., $d = 36 - 50$ nm). The robustness of the laser absorption enhancement in nanowire arrays is accompanied by a similar robustness of the radiation efficiency, which remains relatively high, $\eta_\gamma > 3\%$ (resp. $> 1\%$) for $\hbar\omega > 10$ keV (resp. > 1 MeV) up to $n_{av} = 240n_c$ ($d = 500$ nm). By contrast, the radiation yield from uniform targets decreases rapidly after its maximum: η_γ drops by a factor ~ 2.5 when n_{av} is increased from $24n_c$ to $32n_c$, and falls below 3% for $n_{av} \geq 64n_c$.

If we restrict our analysis to the forward radiation ($\theta_\gamma \leq 30^\circ$), we find that the highest yield into > 1 MeV photons ($\eta_\gamma \simeq 0.4\%$) is provided by a nanowire array of width $d = 36$ nm, yet with little variation ($< 10\%$) in the $36 \leq d \leq 100$ nm range. Also, the highest yield into > 10 keV photons is observed for $d = 300$ nm ($\eta_\gamma \simeq 0.7\%$), with $< 10\%$ variation in the $36 \leq d \leq 300$ nm range.

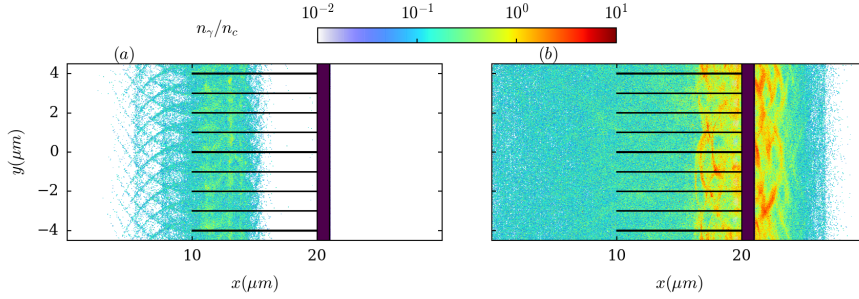


Figure 16. Normalized density (n_γ/n_c) of the high-energy (> 1 MeV) photons (a) before ($t = +13$ fs) and (b) after the reflection ($t = +56$ fs) of the laser pulse off the copper foil at the target backside. The initial target shape is shown in dark red.

3. Radiation enhancement by a reflective substrate

We now investigate whether a more realistic setup, whereby the nanowire array is coated on a solid-density substrate, may substantially improve the synchrotron process. The rationale for this is that, for the parameters (carbon wires with $D = 1 \mu\text{m}$ and $d = 36 - 100$ nm) previously found to yield the highest radiation efficiencies ($\eta_\gamma \geq 8\%$), a sizable fraction of the laser energy (*e.g.*, $\sim 25\%$ at $d = 36$ nm) shines through the target via RSIT. Making this transmitted light reflect off a plasma mirror so as to interact with the hot electrons filling the nanowire array could sustain the synchrotron emission, and hence increase its efficiency.

To test this scenario, we have performed a simulation in which a $1 \mu\text{m}$ -thick copper foil is placed at the backside of a carbon wire array with $D = 1 \mu\text{m}$, $d = 36$ nm and $L = 10 \mu\text{m}$. The Cu ions are initialized with 5+ charge state and a density $n_{\text{Cu}} = 80n_c$. As before, collisional and field ionizations are described. The laser pulse maximum ($10^{22} \text{ W cm}^{-2}$) strikes the Cu foil at $t_r = +33$ fs. For this simulation only, the γ -ray photons ($\hbar\omega \geq 1$ MeV) are advanced (ballistically) on the simulation domain. The evolution of their density is depicted in Figs. 16(a,b). At $t = +13$ fs $< t_r$ [Fig. 16(a)], the wires have rapidly expanded (in the leading edge of the laser) to form a relativistically underdense plasma ($n_e \simeq 17n_c$), in which synchrotron emission occurs volumetrically mainly through RESE, as analyzed in Sec. 2.2. At $t = +56$ fs $> t_r$ [Fig. 16(b)], high-density ($\sim 10n_c$) photon bunches are seen to radiate from the target backside.

The resulting time-integrated energy-angle radiation spectrum is displayed in Fig. 17(b), and compared with that obtained from the sole nanowire array [Fig. 17(a)]. Comparison of the two spectra reveals the generation of two distinct photon groups. The first one originates from the interaction with the expanded wires, and is broadly distributed in the backward direction ($\theta_\gamma = 2 - 3$ rad) with mean energies ~ 0.4 MeV (resp. ~ 2.5 MeV) for $\hbar\omega > 10$ keV (resp. > 1 MeV). The second one follows the reflection of the laser head off the foil, and its interaction with the electrons still accelerated in the laser tail. As already stressed, the quantum parameter is maximized for the forward-moving electrons that stream against the reflected pulse. Consequently, in this emission stage the radiated energy is mainly, but not entirely, forward-directed, as seen by comparing Figs. 17(a) and (b). This secondary emission stage increases the integrated radiation efficiency to $\sim 13\%$ (*vs.* $\sim 10\%$ without

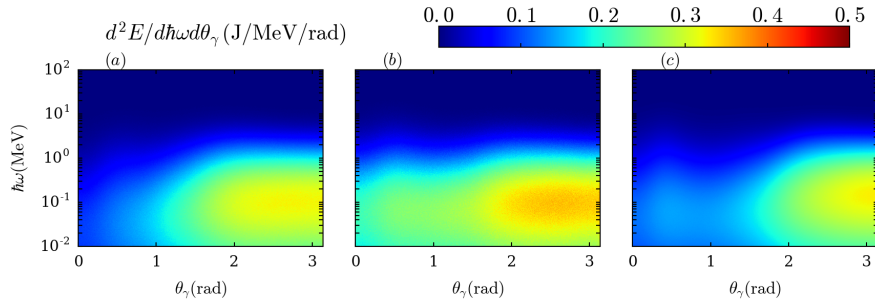


Figure 17. Energy-angle spectrum of the radiated energy for (a) the optimized nanowire array ($d = 36$ nm, $D = 1$ μ m) without substrate, (b) the optimized nanowire array target with substrate, and (c) the optimized (and density-equivalent) uniform plasma ($n_e = 16n_c$). Angles are defined by $\theta_\gamma = \arccos(k_{\gamma,x}/k_\gamma) \in (0, \pi)$. All spectra are integrated over the simulation duration.

substrate, for $\hbar\omega > 10$ keV). Closer analysis reveals that out of the $\sim 26\%$ of laser energy hitting the Cu foil, approximately 13% is further gained by electrons and ions, 3% is converted into photons, and 10% escapes through the target front side.

Finally, we show in Fig. 17(c) the energy-angle spectrum recorded from the optimized uniform-density target ($n_e = 16n_c$), giving a radiation efficiency $\eta_\gamma \sim 11\%$ into > 10 keV photons. It corroborates our previous findings that optimized nanowire arrays and uniform targets yield similar photon distributions. Notable differences, however, are visible: the backward-emission cone angle is slightly narrower, and is complemented by a distinct, albeit weaker, forward emission around $\theta_\gamma \sim \pi/4$ rad.

While the optimized nanowire array with substrate yields the highest radiation conversion efficiency, $\eta_\gamma = 13\%$ (for $\hbar\omega > 10$ keV), its performance falls by an order of magnitude, as does that of the two other types, if we consider only photon energies > 1 MeV and forward emission angles $\leq 30^\circ$ (as would be relevant for, *e.g.*, creating electron-positron pairs in a thicker high- Z substrate): one then obtains $\eta_\gamma \sim 1.2\%$ with a substrate and $\eta_\gamma \simeq 0.9\%$ from the uniform target.

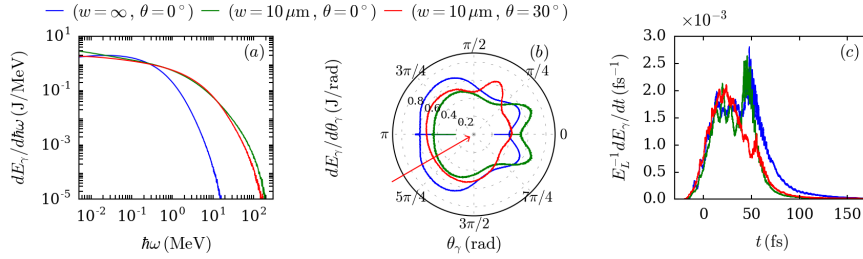


Figure 18. Variations of the synchrotron emission with the laser spot size (w) and incidence angle (θ_0): (a) energy spectra, (b) angle-resolved radiated energy and (c) time-resolved radiated power (normalized to the total laser energy E_L). Each color represents a different case as indicated in the legend of panel (a). $w = \infty$ corresponds to the planar wave case. Angles in (b) are defined as $\theta_\gamma = \arctan(k_{\gamma,y}/k_{\gamma,x}) \in (0, 2\pi)$. The red arrow indicates the $\theta_0 = 30^\circ$ incidence angle. All plotted quantities are integrated over the simulation domain.

4. Effects of a finite focal spot and an oblique incidence angle

All the results of the previous sections correspond to a planar laser wave normally incident on a nanowire array. One may wonder whether they still hold in the more realistic case of a focused, possibly obliquely incident, laser beam. The variations of the synchrotron yield with the laser incidence angle have been recently investigated in Ref. [82], but this study considered planar targets irradiated at a very high laser intensity ($1.3 \times 10^{23} \text{ Wcm}^{-2}$). The strongest emission was found for an incidence angle $\theta_0 \simeq 30^\circ$ and an electron density $n_{av} \simeq 100n_c$. Our goal here is not to extend this comprehensive study to the case of nanowire arrays but, rather, to examine briefly how the use of an obliquely incident, focused laser pulse may alter the properties of the emission compared to the optimal planar-wave configuration. To this end, we have run additional simulations in which the 10^{22} Wcm^{-2} , 30 fs laser pulse has an 8th-order hyper-Gaussian transverse profile of FWHM $w = 10 \mu\text{m}$, and impinges onto the target at an angle $\theta_0 = 0^\circ$ or 30° . The choice of a hyper-Gaussian transverse profile aims at minimizing intensity gradient effects, thus easing comparison with the planar-wave results. The laser electric field is in the xy plane (p polarization). The target consists of the highest-yield nanowire setup ($d = 36 \text{ nm}$, $D = 1 \mu\text{m}$, $L = 10 \mu\text{m}$ with a Cu substrate) as previously identified.

The changes induced by the laser's finite focal spot size and oblique incidence angle on the synchrotron radiation are displayed in Figs. 18(a-c). Since the problem is no longer symmetric relative to the x -axis, the photon emission angles are now defined as $\theta_\gamma = \arctan(k_{\gamma,y}/k_{\gamma,x}) \in (0, 2\pi)$. A striking result [Fig. 18(a)] is that a $10 \mu\text{m}$ laser focal spot leads to a 10-fold increase in the cutoff photon energy, which attains $\hbar\omega_{\text{max}} \simeq 150 - 180 \text{ MeV}$ (weakly dependent on θ_0) compared to $\hbar\omega_{\text{max}} \simeq 16 \text{ MeV}$ for a plane wave. The mean photon energies are also increased, albeit to a lower extent, from $\langle \hbar\omega \rangle \simeq 2.5 \text{ MeV}$ (above 1 MeV) for a plane wave to $\langle \hbar\omega \rangle \simeq 3.5 \text{ MeV}$ in the focused case.

These enhanced photon energies stem from the relativistic self-focusing undergone by the finite-spot laser pulse in the homogenized plasma [83]. This phenomenon is illustrated in Fig. 19, which displays the maps of the magnetic field and electron

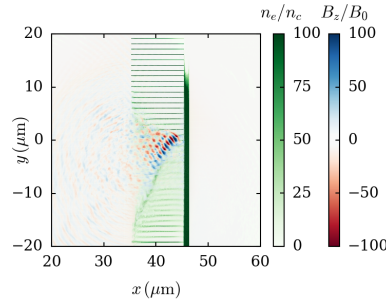


Figure 19. Propagation of the obliquely incident, focused laser pulse with $w = 10 \mu\text{m}$ and $\theta_0 = 30^\circ$: magnetic field (B_z/B_0 , red-blue colormap) and electron density (n_e/n_c , green colormap) at $t = 83 \text{ fs}$ after the on-target laser peak.

density in the $\theta_0 = 30^\circ$ case at $t = 83 \text{ fs}$ after the on-target laser peak. We see that the laser beam has self-focused to a $\sim 2 \mu\text{m}$ spot where it reaches a maximum field strength of $B_z/B_0 \simeq 100$, consistent with the $\sim 75\%$ absorption it has then experienced. The laser self-focusing significantly affects the electron energy spectra, as shown in Fig. 20 at $t = 83 \text{ fs}$. While the electron energy spectra produced by the focused beams show similar temperatures ($T \simeq 65 \text{ MeV}$, such that $dN_e/dE_e \propto \exp(-E_e/T)$) to the planar wave case up to $E_e \simeq 140 \text{ MeV}$, they present additional hotter, high-energy tails, extending up to $E_e \simeq 400 \text{ MeV}$.

As a result, the angle-resolved photon spectra obtained with the focused beams show notable differences with the planar-wave case [Fig 18(b)]. At $\theta_0 = 0^\circ$, the backward emission is reduced while the forward radiation is enhanced and emitted into smaller-angle emission lobes ($\theta_\gamma \simeq \pm 20^\circ$). As for the planar wave, the time-resolved radiated power presents two successive maxima corresponding to the laser interaction with the homogenized nanowires and the substrate [Fig. 18(c)]. The overall conversion efficiency is found to be slightly lower than that observed using a planar wave ($\eta_\gamma \sim 10.2\%$ vs. $\sim 13\%$), with a larger fraction emitted in the forward ($\theta_\gamma < 90^\circ$) direction ($\sim 49\%$ vs. $\sim 42\%$). At $\theta_0 = 30^\circ$, the backward emission is also lowered (though less than at $\theta_0 = 0^\circ$), yet the main difference concerns the forward emission, peaked at angles $\theta_\gamma \simeq 0^\circ$ and $\theta_\gamma \simeq 67^\circ$. Another difference is the much reduced second maximum in the time-resolved radiated power. This follows from the longer penetration length, and hence increased absorption of the obliquely propagating laser pulse across the nanowires, which therefore interacts at a lower intensity with the substrate. This weakened secondary radiation, however, is compensated for by a strengthened radiation throughout the nanowires, thus leading to a total radiation efficiency ($\sim 10.3\%$) equal to that obtained at normal incidence.

Overall, those results show that the salient radiation properties evidenced in the planar-wave case are significantly, but not strongly, affected by using a few nanowires wide focal spot and a moderately oblique incidence angle.

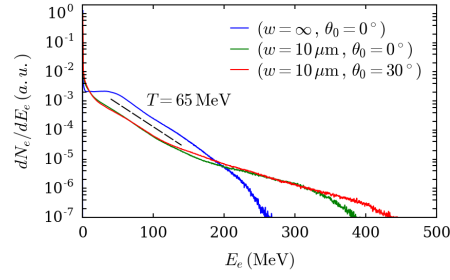


Figure 20. Variations of the electron energy spectra dN_e/dE_e with the laser spot size (w) and incidence angle (θ_0). The best-fitting temperature $T = 65$ MeV is computed in the $40 \leq E_e \leq 140$ MeV range.

Conclusions

Synchrotron radiation from nanowire-array targets irradiated by ultraintense ($10^{21} \leq I \leq 10^{23} \text{ Wcm}^{-2}$), ultrashort (30 fs) laser pulses has been numerically investigated using 2D PIC simulations. We have shown that distinct radiation mechanisms can arise in the course of the interaction, and at various locations in the target depending on its geometry. A main finding is that, under the strong-field conditions studied, the wires rapidly expand during the laser pulse, hence forming a fairly (but not fully) homogenized, relativistically hot plasma. Consequently, the major emission mechanisms (SDE, RESE, TOEE) previously evidenced in uniform-density plasmas [17, 46, 45] also take place in nanowire arrays. Moreover, we have found that the electrostatic reflection of the energized electrons at the target backside and the slowly-decaying magnetostatic fields induced around the wires can provide additional radiation channels. In the case of carbon wires driven at $I = 10^{22} \text{ Wcm}^{-2}$, optimum radiation efficiency, $\eta_\gamma \sim \%$ (resp. $\sim 6\%$) for $\hbar\omega > 10 \text{ keV}$ (resp. $> 1 \text{ MeV}$), is achieved for an interspacing $D \sim 1 \mu\text{m}$ and wire widths $d \sim 36 - 50 \text{ nm}$. In the resulting relativistically transparent ($n_e \sim 20n_c$) plasma, synchrotron emission proceeds through RESE, and is mainly radiated in a large-aperture backward cone. When increasing the wire width and/or decreasing the interwire spacing so that the homogenized plasma becomes overdense, the radiation is increasingly forward-directed due to the then-prevailing SDE. Conversely, decreasing the wire width or increasing the interspacing tends to favor backward radiation processes, *i.e.*, RESE and the backside emission due to refluxing electrons. Although we have not conducted an extensive parametric scan at laser intensities other than 10^{22} Wcm^{-2} , we have found that the radiation efficiency typically increases from $\sim 0.1\%$ at $I = 10^{21} \text{ Wcm}^{-2}$ to $\sim 45\%$ at $I = 10^{23} \text{ Wcm}^{-2}$.

While a $\sim 10\%$ peak radiation efficiency into $> 10 \text{ keV}$ photons is also reported in uniform carbon plasmas of ‘equivalent’ density ($n_{av} = Zn_i d/D$), nanowire arrays are observed to achieve significant ($> 3\%$) radiation yields up to half solid ($240n_c$) average densities. Nanowire arrays therefore prove useful not only as practical means of producing, after fast homogenization, plasma targets of controlled sub-solid density and composition (by varying the array parameters) [83], but also *per se* as robust and efficient high-energy photon sources. Besides, we have shown that the radiation yield can be further boosted (up to $\eta_\gamma \sim 13\%$) by adding a plasma mirror (a micrometric solid foil) at the backside of the array. The influence of a finite laser focal spot ($w = 10 \mu\text{m}$) has also been briefly addressed: the increased laser intensity that results from relativistic self-focusing enhances the production of high-energy electrons, which in turn leads to a slightly more forward-directed and significantly more energetic photon source, with a $\times 1.4$ (resp. $\times 10$) increase in the mean (resp. cutoff) photon energy. Operating with a 30° incidence angle gives very similar results.

To conclude, we remark that our study has assumed a negligible laser prepulse, and therefore that the nanostructure is intact at the arrival of the intense laser pulse. Were the nanostructure to be prematurely destroyed, it would remain worthwhile to adjust its parameters so as to produce a relativistically underdense plasma, and to employ a plasma mirror to enhance the total radiation yield. On the theory side, a limitation of our work, due to computational constraints, is its reduced (2D) geometry. A recent related study [56] points out that the resonant processes responsible for electron energization in nanowire arrays may notably differ between 2D and 3D simulations. This work, however, considers immobile ions and a much weaker intensity

($\sim 6 \times 10^{19} \text{ Wcm}^{-2}$) than ours, so that the array structure is maintained over a longer time. In our case, by contrast, most of the laser interaction takes place as in a fairly uniformized plasma, which should somewhat mitigate the 2D/3D discrepancy highlighted in Ref. [56]. We therefore expect that our major findings, regarding the nature, efficiency and interplay of the relevant emission processes, remain mostly valid when moving to 3D. Finally, we neglected the emission of Bremsstrahlung by the hot electrons, as well as all secondary processes possibly induced by the high-energy photons during their transport, such as electron-positron pair generation or photonuclear reactions. Some of these limitations will be addressed in future works.

Acknowledgments

One of the authors (E. H) was supported by the French National Research Agency project TULIMA (ANR-17-CE30-0033-01) and the US Air Force project AFOSR No. FA9550-17-1-0382. The authors acknowledge support by GENCI, France for awarding up access to HPC resources at TGCC/CCRT (Grant No. 2016-057594 and 2017-057594).

References

- [1] Di Piazza A, Müller C, Hatsagortsyan K Z and Keitel C H 2012 *Rev. Mod. Phys.* **84**(3) 1177–1228
- [2] CILEX, Centre Interdisciplinaire Lumière Extrême <http://cilexsaclay.fr/>
- [3] Jeong T M and Lee J 2014 *Annalen der Physik* **526** 157–172 ISSN 1521-3889
- [4] ELI, Extreme Light Infrastructure <http://www.eli-beams.eu/>
- [5] VULCAN petawatt laser system <https://www.clf.stfc.ac.uk/Pages/Vulcan.aspx/>
- [6] XCELS, Exawatt Center for Extreme Light Studies <http://www.xcels.iapras.ru/>
- [7] Naumova N, Schlegel T, Tikhonchuk V T, Labaune C, Sokolov I V and Mourou G 2009 *Phys. Rev. Lett.* **102**(2) 025002
- [8] Bulanov S V, Echkina E Y, Esirkepov T Z, Inovenkov I N, Kando M, Pegoraro F and Korn G 2010 *Phys. Rev. Lett.* **104** 135003
- [9] Tamburini M, Liseykina T V, Pegoraro F and Macchi A 2012 *Phys. Rev. E* **85**(1) 016407
- [10] Blackburn T G, Ridgers C P, Kirk J G and Bell A R 2014 *Phys. Rev. Lett.* **112**(1) 015001
- [11] Ji L L, Pukhov A, Kostyukov I Y, Shen B F and Akli K 2014 *Phys. Rev. Lett.* **112**(14) 145003
- [12] Wang H Y, Liu B, Yan X Q and Zepf M 2015 *Phys. Plasmas* **22** 033102
- [13] Cole J M, Behm K T, Gerstmayr E, Blackburn T G, Wood J C, Baird C D, Duff M J, Harvey C, Ilderton A, Joglekar A S, Krushelnick K, Kuschel S, Marklund M, McKenna P, Murphy C D, Poder K, Ridgers C P, Samarin G M, Sarri G, Symes D R, Thomas A G R, Warwick J, Zepf M, Najmudin Z and Mangles S P D 2018 *Phys. Rev. X* **8**(1) 011020
- [14] Poder K, Tamburini M, Sarri G, Di Piazza A, Kuschel S, Baird C D, Behm K, Bohlen S, Cole J M, Duff M, Gerstmayr E, Keitel C H, Krushelnick K, Mangles S P D, McKenna P, Murphy C D, Najmudin Z, Ridgers C P, Samarin G M, Symes D, Thomas A G R, Warwick J and Zepf M 2017 *ArXiv e-prints (Preprint 1709.01861)*
- [15] Bell A R and Kirk J G 2008 *Phys. Rev. Lett.* **101**(20) 200403
- [16] Nerush E N, Kostyukov I Y, Fedotov A M, Narozhny N B, Elkina N V and Ruhl H 2011 *Phys. Rev. Lett.* **106**(3) 035001
- [17] Ridgers C P, Brady C S, Ducloux R, Kirk J G, Bennett K, Arber T D, Robinson A P L and Bell A R 2012 *Phys. Rev. Lett.* **108**(16) 165006
- [18] Ji L L, Pukhov A, Nerush E N, Kostyukov I Y, Shen B F and Akli K U 2014 *Phys. Plasmas* **21** 023109
- [19] Zhu X L, Yu T P, Sheng Z M, Yin Y, Turcu I C E and Pukhov A 2016 *Nature Comm.* **7** 13686
- [20] Grismayer T, Vranic M, Martins J L, Fonseca R A and Silva L O 2017 *Phys. Rev. E* **95**(2) 023210
- [21] Jirka M, Klimo O, Vranic M, Weber S and Korn G 2017 *Sci. Reports* **7** 15302
- [22] Liang E 2013 *High. Energ. Dens. Phys.* **9** 425–427
- [23] Chen H, Fiuza F, Link A, Hazi A, Hill M, Hoarty D, James S, Kerr S, Meyerhofer D D, Myatt J, Park J, Sentoku Y and Williams G J 2015 *Phys. Rev. Lett.* **114** 215001

- [24] Lobet M, Ruyer C, Debayle A, d'Humières E, Grech M, Lemoine M and Gremillet L 2015 *Phys. Rev. Lett.* **115**(21) 215003
- [25] Kirk J G, Bell A R and Arka I 2009 *Plasma Phys. Control. Fusion* **51** 085008
- [26] Phuoc K T, Corde S, Thauray C, Malka V, Tafzi A, Goddet J P, Shah R C, Sebban S and Rousseau A 2012 *Nature Photon.* **6** 308-311
- [27] Chen S, Powers N D, Ghebregziabher I, Maharjan C M, Liu C, Golovin G, Banerjee S, Zhang J, Cunningham N, Moorti A, Clarke S, Pozzi S and Umstadter D P 2013 *Phys. Rev. Lett.* **110**(15) 155003
- [28] Yan W, Fruhling C, Golovin G, Luo D H J, Zhang P, Zhao B, Zhang J, Liu C, Chen M, Chen S, Banerjee S and Umstadter D 2013 *Nature Photon.* **7** 796-800
- [29] Powers N D, Ghebregziabher I, Golovin G, Liu C, Chen S, Banerjee S, Zhang J and Umstadter D P 2014 *Nature Photon.* **8** 28-31
- [30] Sarri G, Corvan D J, Schumaker W, Cole J M, Di Piazza A, Ahmed H, Harvey C, Keitel C H, Krushelnick K, Mangles S P D, Najmudin Z, Symes D, Thomas A G R, Yeung M, Zhao Z and Zepf M 2014 *Phys. Rev. Lett.* **113**(22) 224801
- [31] Yu C, Qi R, Wang W, Liu J, Li W, Wang C, Zhang Z, Liu J, Qin Z, Fang M, Feng K, Wu Y, Tian Y, Xu Y, Wu F, Leng Y, Weng X, Wang J, Wei F, Yi Y, Song Z, Li R and Xu Z 2016 *Sci. Reports* **6** 29518
- [32] Lobet M, Davoine X, d'Humières E and Gremillet L 2017 *Phys. Rev. Accel. Beams* **20**(4) 043401
- [33] Blackburn T G, Ilderton A, Murphy C D and Marklund M 2017 *Phys. Rev. A* **96**(2) 022128
- [34] Birdsall C K and Langdon A B 2004 *Plasma Physics Via Computer Simulation Series in Plasma Physics* (New York: Taylor & Francis)
- [35] Zhidkov A, Koga J, Sasaki A and Uesaka M 2002 *Phys. Rev. Lett.* **88**(18) 185002
- [36] Tamburini M, Pegoraro F, Di Piazza A, Keitel C H and Macchi A 2010 *New J. Phys.* **12** 123005
- [37] Ducloux R, Kirk J G and Bell A R 2011 *Plasma Phys. Control. Fusion* **53** 015009
- [38] Capdessus R, d'Humières E and Tikhonchuk V T 2012 *Phys. Rev. E* **86**(3) 036401
- [39] Chen M, Esarey E, Geddes C G R, Schroeder C B, Plateau G R, Bulanov S S, Rykovanov S and Leemans W P 2013 *Phys. Rev. ST Accel. Beams* **16**(3) 030701
- [40] Vranic M, Martins J L, Vieira J, Fonseca R A and Silva L O 2014 *Phys. Rev. Lett.* **113**(13) 134801
- [41] Gonoskov A, Bastrakov S, Efimenko E, Ilderton A, Marklund M, Meyerov I, Muraviev A, Sergeev A, Surmin I and Wallin E 2015 *Phys. Rev. E* **92**(2) 023305
- [42] Lobet M, d'Humières E, Grech M, Ruyer C, Davoine X and Gremillet L 2016 *J. Phys. Conf. Ser.* **688** 012058
- [43] Wallin E, Gonoskov A and Marklund M 2015 *Phys. Plasmas* **22** 033117
- [44] Niel F, Riconda C, Amiranoff F, Ducloux R and Grech M 2017 *ArXiv e-prints (Preprint 1707.02618)*
- [45] Chang H X, Qiao B, Zhang Y X, Xu Z, Yao W P, Zhou C T and He X T 2017 *Phys. Plasmas* **24** 043111
- [46] Brady C S, Ridgers C P, Arber T D, Bell A R and Kirk J G 2012 *Phys. Rev. Lett.* **109**(24) 245006
- [47] Brady C S, Ridgers C P, Arber T D and Bell A R 2014 *Phys. Plasmas* **21** 033108
- [48] Stark D J, Toncian T and Arefiev A V 2016 *Phys. Rev. Lett.* **116**(18) 185003
- [49] Huang T W, Zhou C T, Zhang H, Wu S Z, Qiao B, He X T and Ruan S C 2017 *Appl. Phys. Lett.* **110** 021102
- [50] Pan K Q, Zheng C Y, Wu D, Cao L H, Liu Z J and He X T 2015 *Appl. Phys. Lett.* **107** 183902
- [51] Zhu X L, Yin Y, Yu T P, Shao F Q, Ge Z Y, Wang W Q and Liu J J 2015 *New J. Phys.* **17** 053039
- [52] Liu J J, Yu T P, Yin Y, Zhu X L and Shao F Q 2016 *Opt. Express* **24** 15978-15986
- [53] Iwata N, Nagatomo H, Fukuda Y, Matsui R and Kishimoto Y 2016 *Phys. Plasmas* **23** 063115
- [54] Yi L, Pukhov A, Luu-Thanh P and Shen B 2016 *Phys. Rev. Lett.* **116**(11) 115001
- [55] Andreev A A and Platonov K Y 2016 *IEEE J. Quant. Electron.* **46** 109
- [56] Lecz Z and Andreev A 2017 *Phys. Plasmas* **24** 033113
- [57] Wang W M, Sheng Z M, Gibbon P, Chen L M, Li Y T and Zhang J 2017 *ArXiv e-prints (Preprint 1710.11356)*
- [58] Zhao Z, Cao L, Cao L, Wang J, Huang W, Jiang W, He Y, Wu Y, Zhu B, Dong K, Ding Y, Zhang B, Gu Y, Yu M Y and He X T 2010 *Phys. Plasmas* **17** 123108
- [59] Ovchinnikov A, Kostenko O, Chefonov O, Rosmej O, Andreev N, Agranat M, Duan J, Liu J and Fortov V 2011 *Laser & Part. Beams* **29** 249-254
- [60] Mondal S, Chakraborty I, Ahmad S, Carvalho D, Singh P, Lad A D, Narayanan V, Ayyub P, Kumar G R, Zheng J and Sheng Z 2011 *Phys. Rev. B* **83**(3) 035408

- [61] Ivanov K A, Gozhev D A, Rodichkina S P, Makarov S V, Makarov S S, Dubatkov M A, Pikuz S A, Presnov D E, Paskhalov A A, Eremin N V, Brantov A Vand Bychenkov V Y, Volkov R V, Timoshenko V Y, Kudryashov S I and Savel'ev A B 2017 *Appl. Phys. B* **123** 252 ISSN 1432-0649
- [62] Hollinger R, Bargsten C, Shlyaptsev V N, Kaymak V, Pukhov A, Capeluto M G, Wang S, Rockwood A, Wang Y, Townsend A, Prieto A, Stockton P, Curtis A and Rocca J J 2017 *Optica* **4** 1344–1349
- [63] Ji Y, Jiang G, Wu W, Wang C, Gu Y and Tang Y 2010 *Appl. Phys. Lett.* **96** 041504
- [64] Chatterjee G, Singh P K, Ahmed S, Robinson A P L, Lad A D, Mondal S, Narayanan V, Srivastava I, Koratkar N, Pasley J, Sood A K and Kumar G R 2012 *Phys. Rev. Lett.* **108**(23) 235005
- [65] Tian Y, Liu J, Wang W, Wang C, Lu X, Leng Y, Liang X, Li R and Xu Z 2014 *Plasma Phys. Control. Fusion* **56** 075021
- [66] Purvis M A, Shlyaptsev V N, Hollinger R, Bargsten C, Pukhov A, Prieto A, Wang Y, Luther B M, Yin L, Wang S and Rocca J J 2013 *Nature Photon.* **7** 796-800
- [67] Bargsten C, Hollinger R, Capeluto M G, Kaymak V, Pukhov A, Wang S, Rockwood A, Wang Y, Keiss D, Tommasini R, London R, Park J, Busquet M, Klapisch M, Shlyaptsev V N and Rocca J J 2017 *Sci. Adv.* **3**
- [68] Khaghani D, Lobet M, Borm B, Burr L, Gärtner F, Gremillet L, Movsesyan L, Rosmej O, Toimil-Molares M E, Wagner F and Neumayer P 2017 *Sci. Reports* **7** 11366
- [69] Bin J H, Yeung M, Gong Z, Wang H Y, Kreuzer C, Zhou M L, Streeter M J V, Foster P S, Cousens S, Dromey B, Meyer-ter Vehn J, Zepf M and Schreiber J 2018 *Phys. Rev. Lett.* **120**(7) 074801
- [70] Cristoforetti G, Londrillo P, Singh P K, Baffigi F, D'Arrigo G, Lad A D, Milazzo R G, Adak A, Shaikh M, Sarkar D, Chatterjee G, Jha J, Krishnamurthy M, Kumar G R and Gizzi L A 2017 *Sci. Reports* **7** 1479
- [71] Cao L, Gu Y, Zhao Z, Cao L, Huang W, Zhou W, He X T, Yu W and Yu M Y 2010 *Phys. Plasmas* **17** 043103
- [72] Cao L, Gu Y, Zhao Z, Cao L, Huang W, Zhou W, Cai H B, He X T, Yu W and Yu M Y 2010 *Phys. Plasmas* **17** 103106
- [73] Kaymak V, Pukhov A, Shlyaptsev V N and Rocca J J 2016 *Phys. Rev. Lett.* **117**(3) 035004
- [74] Sokolov I V, Naumova N M, Nees J A, Mourou G A and Yanovsky V P 2009 *Phys. Plasmas* **16** 093115
- [75] Brady C S, Ridgers C P, Arber T D and Bell A R 2013 *Plasma Phys. Control. Fusion* **55** 124016
- [76] Jiang S, Ji L L, Audesirk H, George K M, Snyder J, Krygier A, Poole P, Willis C, Daskalova R, Chowdhury E, Lewis N S, Schumacher D W, Pukhov A, Freeman R R and Akli K U 2016 *Phys. Rev. Lett.* **116**(8) 085002
- [77] Wilks S C, Kruer W L, Tabak M and Langdon A B 1992 *Phys. Rev. Lett.* **69**(9) 1383–1386
- [78] Fiuza F, Stockem A, Boella E, Fonseca R A, Silva L O, Haberberger D, Tochitsky S, Gong C, Mori W B and Joshi C 2012 *Phys. Rev. Lett.* **109**(21) 215001
- [79] Weng S M, Murakami M, Mulser P and Sheng Z M 2012 *New J. Phys.* **14** 063026
- [80] Ji L, Pukhov A, Nerush E, Kostyukov I, Akli K and Shen B 2014 *Eur. Phys. J. Spec. Top.* **223** 1069–1082 ISSN 1951-6401
- [81] Siminos E, Grech M, Svedung Wettervik B and Fülöp T 2017 *New J. Phys.* **19** 123042
- [82] Serebryakov D A and Nerush E N 2016 *Quantum Electron.* **46** 299
- [83] Bin J H, Ma W J, Wang H Y, Streeter M J V, Kreuzer C, Kiefer D, Yeung M, Cousens S, Foster P S, Dromey B, Yan X Q, Ramis R, Meyer-ter Vehn J, Zepf M and Schreiber J 2015 *Phys. Rev. Lett.* **115**(6) 064801